Quantifying ageing effects in thermochromic liquid crystal thermography as applied to transient convective heat transfer experiments

Les, C., Brend, M. A., Bonham, C., Carrotte, J. F.

Department of Aeronautical and Automotive Engineering, Loughborough University, Loughborough, LE11 3TU, UK

E-mail: c.bonham@lboro.ac.uk

Abstract. Thermochromic liquid crystal (TLC) thermography is used in transient heat transfer experiments to determine distributions of convective heat transfer coefficient (HTC) inside models of internally cooled gas turbine engine components. As these components become more geometrically complex, the application of TLC thermography becomes increasingly challenging and additional sources of experimental uncertainty grow to be significant. The present work quantifies the uncertainties introduced by TLC ageing using a state-of-the-art imaging system and a new post-processing methodology that are optimised for the intensity-based method of analysing TLC data. A coating comprising multiple TLCs with different active temperature ranges is considered and subject to 33 repeated thermal cycles. These repeated cycles are shown to increase the random and systematic uncertainties in the TLC measurements, resulting in consequent increases in the uncertainties associated with calculated HTCs. Increases in systematic uncertainty are caused by reflectance in the measured wavelength band moving to different temperatures, while increases in random uncertainty are related to changes in individual crystals or crystal clusters with ageing. Approaches to calibrating out increases in systematic uncertainty are proposed and recommended, but increases in random uncertainty will always persist unless the TLC coating is removed and reapplied.

Keywords: thermochromic liquid crystals, heat transfer, uncertainty, ageing
Submitted to: *Meas. Sci. Technol.*

1. Introduction

To reduce specific fuel consumption, gas turbine engine manufacturers have moved towards increasingly aggressive engine cycles, where the high mainstream and coolant temperatures make cooling system design challenging. This situation has been worsened by the recent introduction of lean burn combustion systems, which offer lower NOx emissions but reduce the overall flow rate of air available for cooling [1]. Today, these challenges are leading to the development of increasingly complex internal cooling schemes characterised by long intersecting passages that include either roughness elements or impinging jets to maximise convective efficiency. A novel example is provided by Batstone [2], who considered so-called dendritic cooling systems comprised of multiple interconnected, bifurcated passages. The application of such geometries has been facilitated by recent advances in manufacturing technologies, which have expanded the available design space by permitting intricate features to be employed cost effectively [3].

Knowledge of convective heat transfer coefficient (HTC) distributions inside internal cooling passages is important for predicting component metal temperatures, which must be kept to within allowable limits to achieve adequate service life. Thermochromic liquid crystal (TLC) thermography has become a well-established method of measuring these HTC distributions in transient heat transfer experiments at near atmospheric conditions (see for example [4], [5], [6] and [7]). In these experiments, a thin layer of TLC is applied to a scale model of the cooling passages and a camera used to record the TLC colour-play following a sudden change in flow temperature. Since the TLC selectively reflects shorter wavelengths of light with increasing temperature, the colour-play can be used to determine the temperature history of the model surface. Using this information, HTCs can then be calculated by solving the Fourier equation for conduction in a wall subject to a convective boundary condition. For a one-dimensional, infinitely thick flat plate exposed to a step change in flow temperature [8]:

$$\frac{T_w(t) - T_i}{T_\infty - T_i} = 1 - e^{\alpha^2} erfc(\alpha) \tag{1}$$

where

$$\alpha = h\sqrt{\frac{t}{\kappa}} \tag{2}$$

and

$$\kappa = \rho C k \tag{3}$$

As internal cooling schemes become increasingly complex, the application of TLC thermography to determine HTC distributions becomes ever more challenging. For example, the reflected light return can suffer from low signal to noise ratio (SNR) due to factors including glare, stray reflections and the need to view through multiple semi-transparent walls. Furthermore, local (pixel by pixel) in-situ calibrations of

the TLC's colour-temperature response are impractical, meaning that variations in illumination intensity, viewing angle and TLC film thickness cannot be taken into account. These factors can be mitigated to some extent by adopting intensity-based methods in preference to hue-based methods for analysing the TLC colour-play [9]. Intensity methods are more sensitive to weak signals, which possess very low colour saturation and lead to low SNR in hue. They are also more insensitive to spatial non-uniformities and so allow a single-point calibration to be applied to the entire model surface with better accuracy [10]. For these reasons, an intensity method that uses peak detection in the green portion of the visible spectrum has been employed in this work [11].

A further difficulty with complex cooling geometries arises from the requirement to view the TLC coated surfaces from multiple locations in order to determine the complete HTC distribution. Without expanding the imaging system to include multiple cameras, this requires experiments to be repeated with the camera positioned in different locations. This raises questions over TLC ageing, which has previously been reported to alter the colour-temperature calibration and reduce the reflected light intensity [12] [13]. Under these conditions, surface temperature uncertainties increase, reducing the accuracy of calculated HTCs. TLC ageing can occur from exposure to ultra-violet (UV) radiation, but in practice this is reduced by encapsulating the crystals in protective micro-spheres [14] and viewing the surface through a semi-transparent wall (e.g. acrylic) that acts as an effective UV filter [12]. TLC ageing has also been linked to thermal cycling, particularly at temperatures above the upper clearing point where the TLC becomes an isotropic liquid [13]. Such temperature conditions are more likely to occur in complex geometries due to large spatial variations in HTC, which may result in regions of high heat transfer exceeding the TLC clearing temperature before low heat transfer regions have been activated.

This paper seeks to quantify the impact of TLC ageing on uncertainties in surface temperature and hence derived HTCs. Specifically, a coating comprising multiple TLCs with different active temperature ranges is considered. This represents an advance on the single TLC ageing studies that have previously been reported [12] [13]. Multiple TLC coatings are particularly suited to complex geometries with large spatial variations in HTC, since they present an opportunity to reduce uncertainties introduced by the exceptionally short/long TLC activation times associated with regions of high/low heat transfer [9]. However, understanding the ageing behaviour of the different TLCs is important, since the different start temperatures may correlate to different levels of uncertainty. In order to isolate ageing effects from other sources of experimental uncertainty, significant attention is given to the experimental measurement system and data processing techniques. This includes the development of a new imaging system for subsequent use in determining HTCs in complex cooling geometries, as well as a robust methodology for identifying intensity peaks in TLC data.

2. Experimental Approach

In order to distinguish ageing effects from other sources of experimental uncertainty, careful consideration has been given to the experimental approach employed. The design of the thermal cycling equipment has been based on the work of Terzis [9], which represents an advance on other TLC calibration facilities that have previously been used to investigate TLC uncertainties [13], [12]. A monochrome imaging system for recording the TLC colour-play has also been specifically developed, which offers significant advantages compared to the white light illumination and colour camera combination commonly reported in the literature (see for example [15]).

2.1. Thermal cycling equipment

Figure 1 shows the equipment used to thermally cycle the TLC, which was specifically selected to provide good surface temperature uniformity [9]. The apparatus consisted of an isothermal copper block that was partially submerged in a bath of electrically heated, de-ionized water. The water temperature could be controlled in the range $20 - 100\,^oC$ using a Haake DL30 circulator and a water temperature uniformity of $0.1\,^oC$ achieved. The TLC coating was applied to an optically clear acrylic disc and placed on the top surface of the copper block. Good thermal contact across the copper-TLC interface was ensured by adding a thin layer of thermal grease with conductivity $10\,W/mK$. The maximum temperature difference across the thermal grease was estimated to be less than $0.01\,^oC$ based on a one-dimensional heat conduction calculation. A ring of Rohacell insulation ($0.03\,W/mk$) was also placed around the acrylic disc to minimise any heat transfer to the surrounding air. To provide a means of calibrating the TLC colour-play, three T-type thermocouples (OMEGA $13\,\mu m$ foil type) were adhered to the top face of the copper block to measure its surface temperature. These thermocouples have a time constant of $\sim 1\,ms$, which is the same order of magnitude as the time response of the TLCs [13]. The temperature measurements were acquired at a rate of $3\,Hz$ using a National Instruments NI-9214 thermocouple module. The thermocouples were statically calibrated against a Pt100 thermometer to minimise systematic errors in the measurements. The repeatability of the measurements was calculated as $0.006\,^oC$ from the standard deviation of repeated static calibrations and applying the Student t-distribution. This is the measurement system uncertainty of interest, since it is the relative temperature change between thermal cycles that is important rather than the absolute temperature accuracy.

2.2. Imaging system

A new TLC imaging system was specifically developed for this work and consisted of a monochrome camera and light source. Images were recorded using an Imperx Bobcat B1641 machine vision camera with an interline transfer CCD. To the author's knowledge, this specific type of camera has not previously been used for TLC thermography but

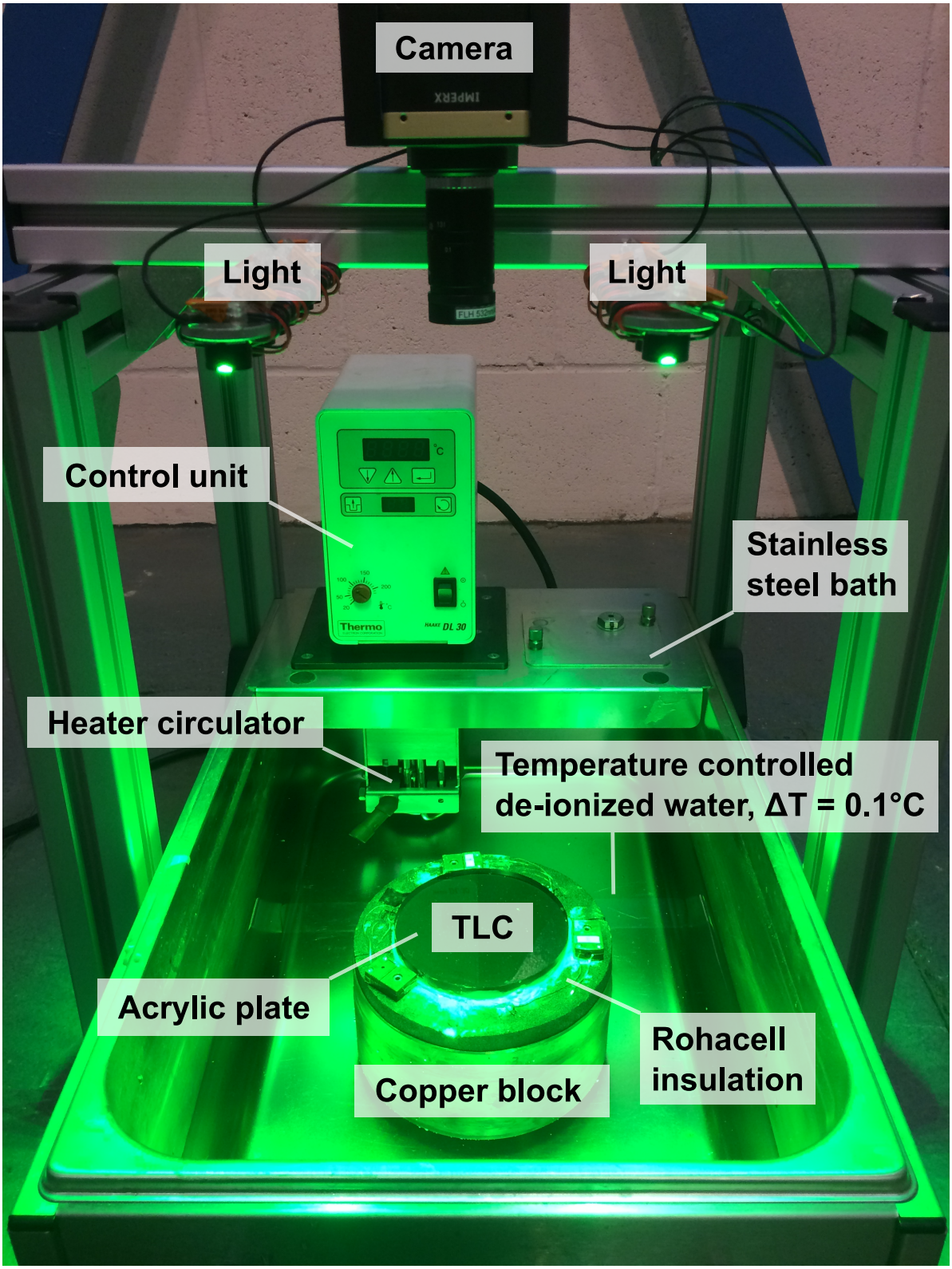

Figure 1. Illustration of the equipment used to thermally cycle the TLC

offers several benefits for both the current study and future applications to complex geometries. The vast majority of imaging detectors reported in the literature are progressive scan (see for example [16, 17, 11, 18, 19, 20]), meaning that pixels are exposed and read out sequentially from the detector array, resulting in a timing error between adjacent pixels. For interlaced video sensors that still see use in the field (see [21, 16, 22, 13, 17, 12, 18]) this is particularly important as odd and even rows in the array are exposed sequentially. An electronic global shutter eliminates these issues, exposing all pixels almost simultaneously (to within a few 10s of nanoseconds). Further benefits arise from the use of interline transfer CCDs, for which continuous frame rates are effectively constrained by data transfer bandwidths. This presents an opportunity to trade-off image resolution for frame-rate. Increased frame rates are desirable for reducing timing uncertainties, which can become significant for the short TLC activation times associated with regions of high heat transfer. For example, Terzis [9] quotes temperature uncertainties of $\sim 5\%$ for TLC activation times of the order $1\,s$ with a timing accuracy of $100\,ms$. Using a camera with an interline transfer CCD could decrease the timing uncertainty to that of the crystal's molecular response time, which is a few milliseconds for the encapsulated chiral nematic TLCs considered here [13].

Since a monochrome detector is being used, some form of filtering is desirable in order to restrict the integrated wavelengths to the green portion of the visible spectrum. A hard coated interference bandpass filter with a 532 nm centre wavelength and a 4 nm passband (Thorlabs FLH532-4) has therefore been fitted to the camera lens. This completely eliminates contributions to the measured signal from ambient lighting in the laboratory, even under normal lighting conditions. However, since narrow passband filters only transmit a small portion of the incident light, measured signals are attenuated. For this reason, illumination was provided by two LED arrays (OSRAM OSLON SSL 150) that were driven in current limited mode to allow fine-tuning of the emitted light intensity and so the TLC reflected light return. An LED design that did not produce light through UV stimulation of a phosphor was specifically chosen to eliminate any possible light-source induced ageing.

2.3. Surface preparation

The TLC coating comprised of three Hallcrest narrow-band microencapsulated TLCs: G35C1W, R38C1W and R40C1W. These have an active temperature range of $1\,^oC$, with colour start temperatures of $35, 38, 40\,^oC$ respectively. This combination of TLCs has previously been used for investigations of impinging jet heat transfer and is therefore well suited to applications involving large spatial HTC variations in complex geometries [9]. The three TLCs were sprayed on to the surface of the acrylic disc using an airbrush and were applied in order of decreasing crystal indication temperature (see Figure 2). For each TLC, a film thickness of $20\,\mu m$ was used since this has been reported to provide high colour-play SNR [13], whilst also limiting temperature gradients across the film due to conduction [12]. The finished TLC coating was topped with a $15\,\mu m$ layer of matte

black paint to provide good background contrast.

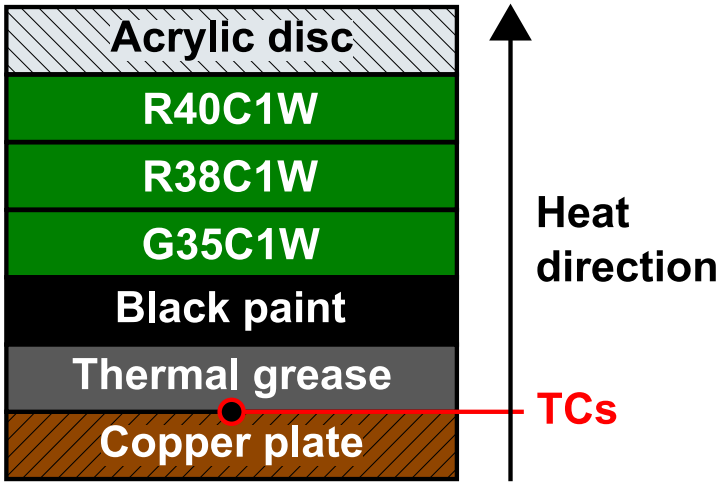

Figure 2. Diagram showing the order of TLC films applied the acrylic disc test piece.

2.4. Experimental procedure

The TLC coating was thermally cycled by raising the water bath temperature from 30 to 45 ^oC. Based on surface thermocouple measurements, the corresponding temperature of the copper block increased at a rate of $\sim 0.025\,^oC/s$, reaching the target of 45 ^oC after $\sim$ 10 minutes. During this time, the initially inactive TLCs displayed their entire colour-play before returning to an almost inactive state. Compared to transient heat transfer experiments performed on scaled models of internal cooling passages (see for example [4]), the rate of heating used here is approximately an order of magnitude lower. This is a consequence of the high thermal capacity of the water bath and copper block, which provides good temperature uniformity across the measurement surface. However, the 30 ^oC start temperature and 15 ^oC temperature rise are broadly representative of such experiments, where initial conditions are determined by the ambient temperature and modest temperature changes are needed to correspond with the TLC active temperature range. This range is limited to between 0.5 and 30 ^oC, with crystal start temperatures further constrained to between -30 and 120 ^oC [13].

During each thermal cycle, images of the TLC colour-play were captured with an exposure of 10 ms at a frame rate of 3 Hz, which was nominally matched to the sampling rate of the surface thermocouples. An automatic triggering system was in place to synchronize the camera images and thermocouple measurements to within one data point (i.e. 0.33 s or 0.0087 ^oC). When combined with the measurement system uncertainty using a root-sum-square method, this increases the overall temperature measurement uncertainty to 0.011 ^oC. Image data was streamed over CameraLink to a Euresys full frame grabber, while thermocouple data was logged using LabView®. Tests were repeated over a period of two months, with a total of 33 thermal cycles performed at an average rate of 1 test every 2-3 days. Multiple tests could not be performed in a

single day due to the time required to return the water bath and cooper block to the cycle start temperature. However, in the authors' experience the interval between tests as well as the overall test duration is not unrepresentative of a measurement campaign on a complex cooling geometry, where multiple tests are performed at different viewing angles in order to generate full surface HTC distributions. Over the duration of the 33 tests, the TLC coated disc remained in-situ on the surface of the copper block, where it was effectively stored at ambient conditions when not in use. A thick matte black curtain was used to cover the experimental equipment and eliminate the possibility of TLC ageing caused by exposure to ambient lighting.

3. Data analysis

Post-processing of the TLC images was performed in MATLAB®. The images were cropped to a central circle of $20mm$ diameter, as shown in Figure 3. Cropping in this manner ensured the surface thermocouple junctions were just outside the region of interest (ROI) and did not influence the TLC colour-play data. The total number of pixels inside the ROI was approximately 30000. At each pixel location, the raw intensity profile was analysed and the peak value used to calibrate the TLC colour-play against surface temperature [11]. Most simply, the peak location may be identified via the maximum recorded intensity. However, high frequency noise can cause random variations at the summit location that lead to slight variations in the corresponding surface temperature. In order to reliably attribute small shifts in summit location to TLC ageing, a more accurate method of peak detection is therefore required. Accordingly, a new methodology for identifying intensity peaks in TLC data has been developed, which involves analysing the measurements in three distinct stages that are described in Sections 3.1 to 3.3.

3.1. Adaptive filter design

The isothermal copper block shown in Figure 1 is specifically designed to provide a uniform surface temperature distribution across the TLC-coated acrylic disc [9]. Given the inherent dependence of TLC spectral reflectivity upon temperature, it is therefore reasonable to assume relatively low spatial variations in the measured intensity profile. This assumption is supported by the data shown in Figure 4, which is a comparison between intensity peaks recorded at individual pixel locations and spatially averaged data across the entire ROI. The first pass parameterisation of the TLC peak was therefore performed using spatially averaged data. Spatial averaging across such a large number of pixels removes almost all of the high frequency noise present in the instantaneous measurements and so the maxima and minima of the peak are easily found. From these, the width of the average peak at half-height is determined, z, with half-height being defined as the midpoint between the maxima and minima. The half-height width is then used to define a Gaussian filter, with frequency cut-off of $1/4z$.

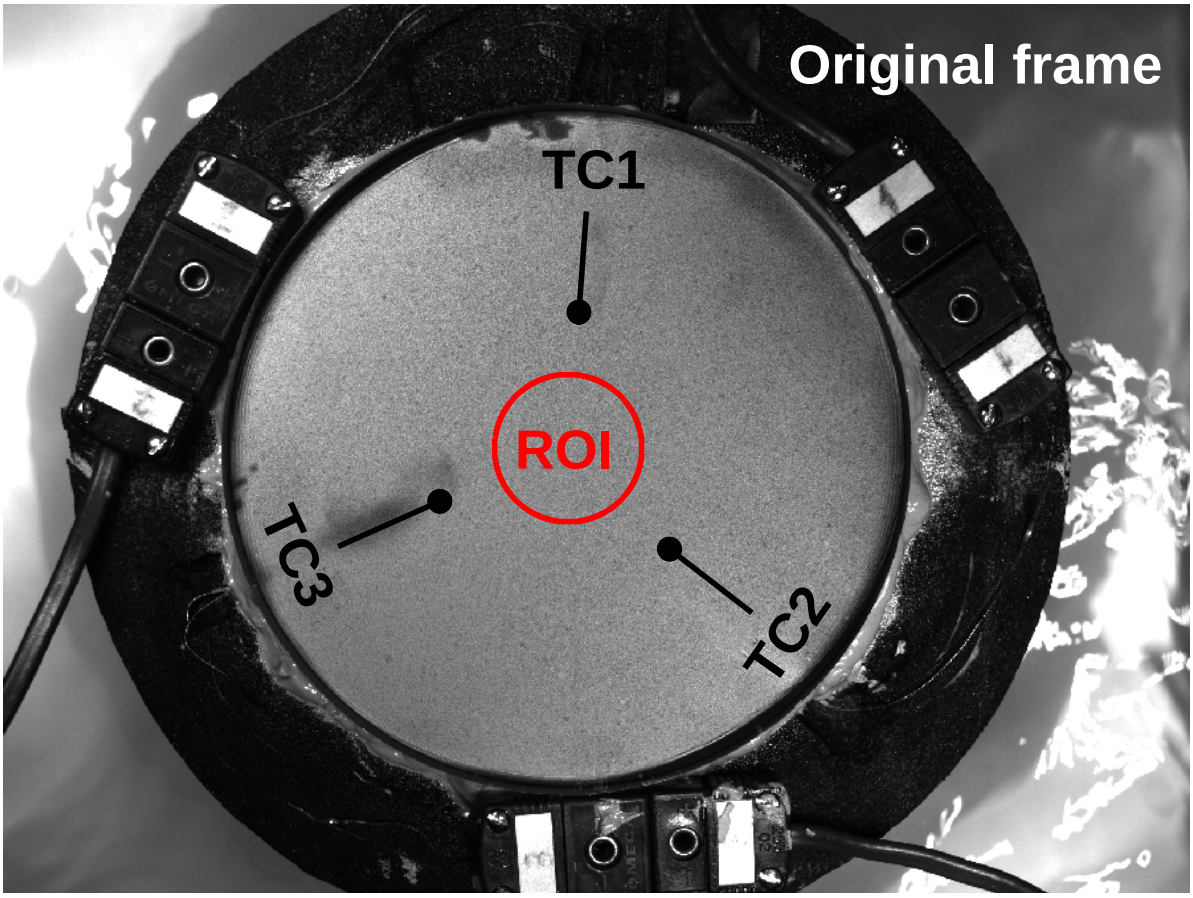

Figure 3. Post-processing of TLC images

Defining a low-pass filter adaptively in this way maintains a consistent level of trade-off between the attenuation of undesirable high-frequency noise and equally undesirable elimination of measured data.

3.2. Low-pass filtering

The low-pass filter defined by the half-height width of the spatially averaged peak is next used to filter the intensity profile measured at each individual pixel within the ROI. From this filtered signal, the maxima, minima and summit location of the peak at each pixel location were found. Any filtered peaks with height lower than 10 counts were rejected and marked as invalid. Similarly, peaks with maxima lower than 10% of the value of the spatially averaged peak height were also rejected and marked as invalid. The upper quartile of the raw signal was then selected. The boundary of the upper quartile is defined as 75% of the distance from the minima to the maxima found from the filtered data, illustrated in Figure 5. The intersections between this upper quartile boundary and the raw intensity data were then found in temperature coordinates. These parameters were subsequently used to define the portion of raw unfiltered data to be regressed.

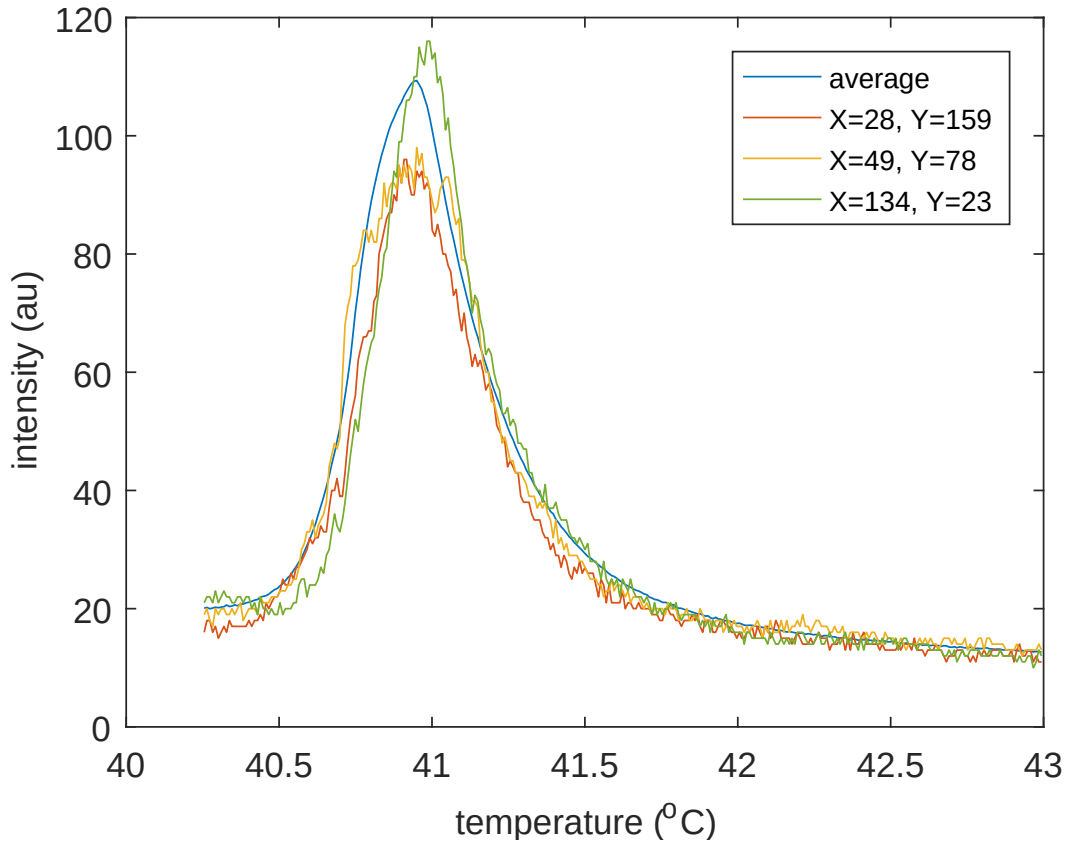

Figure 4. Intensity profiles extracted from individual pixel locations, compared to a spatially averaged intensity profile across the ROI.

3.3. Summit location regression

To a first order, Gaussian functions appear to be an appropriate model for fitting peaks in TLC intensity data, since they have a single summit location and non-linear gradient. However, TLC peaks are rarely symmetric, as can be seen from the data plotted in Figure 4. For the accurate determination of summit locations, an asymmetric model that permits some degree of skewness is therefore desirable. The fitting of asymmetric, skewed peaks is of importance across a variety of fields, in particular the field of chromatography for biological and molecular analysis [23]. As such, a bewildering number of potentially appropriate models have been reviewed [24]. For the case of TLC intensity peaks, variations are expected in height, width, summit location and skewness. As some noise is present in the intensity data, the ideal model will have few degrees of freedom in excess of those listed, so that components are not unnecessarily fitted to noise in the data. Additionally, the ideal model will directly parameterise the coefficients described and have a single maximum. It is also desirable that regression of the selected model be relatively fast, so that it may be exploited for measurements on complex geometries where the ROI is large and so very large numbers of peak detections are required.

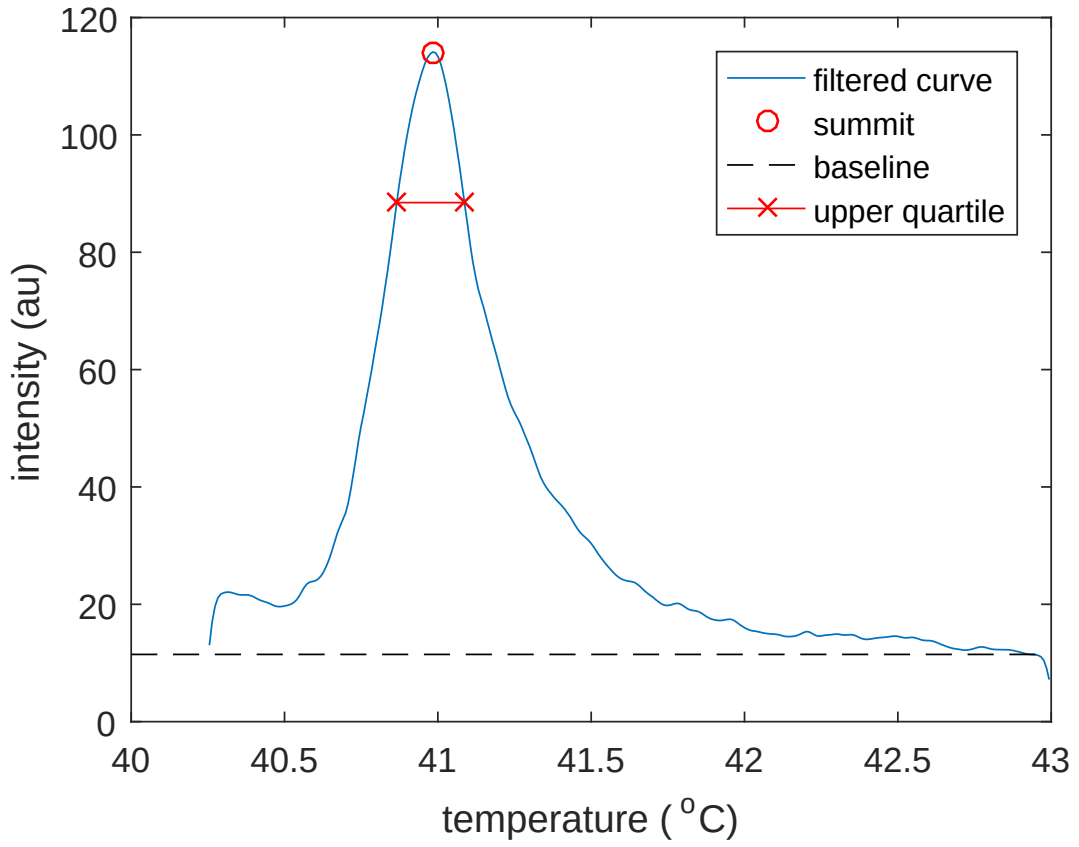

Figure 5. Parameterisation of the low-pass filtered intensity data for a single TLC peak. The parameters are used to define the portion of raw unfiltered data to be regressed.

Four candidate models that nominally fit these criteria above have been selected for comparison: a Gaussian function provides a datum for the current practice in TLC analysis; the Lorentzian function or Cauchy distribution provides a similar symmetric formulation with a less aggressive asymptote; the bi-Gaussian provides an early example of an asymmetric peak model, with the left and right sides of the summit location modelled as separate Gaussian functions [25]; the modified asymmetric pseudo-Voigt (mAPV) provides a recent improvement to the traditional pseudo-Voigt formulation [26] with performance gains on the bi-Gaussian demonstrated by modelling the left and right sides of the summit as separate sums of Gaussian and Lorentzian functions. Because of the high level of scatter in the raw data and the underlying similarity to the spatially averaged peak, a meaningful comparison of the goodness of the models has been performed using the average intensity data shown in Figure 4. All models were fitted using a non-linear optimiser, minimising the square of residuals. The models were regressed using a gradient-descent optimiser, with the mAPV additionally regressed using a genetic algorithm optimiser. The evaluated fitted models are shown alongside the spatially averaged peak intensity data in Figure 6.

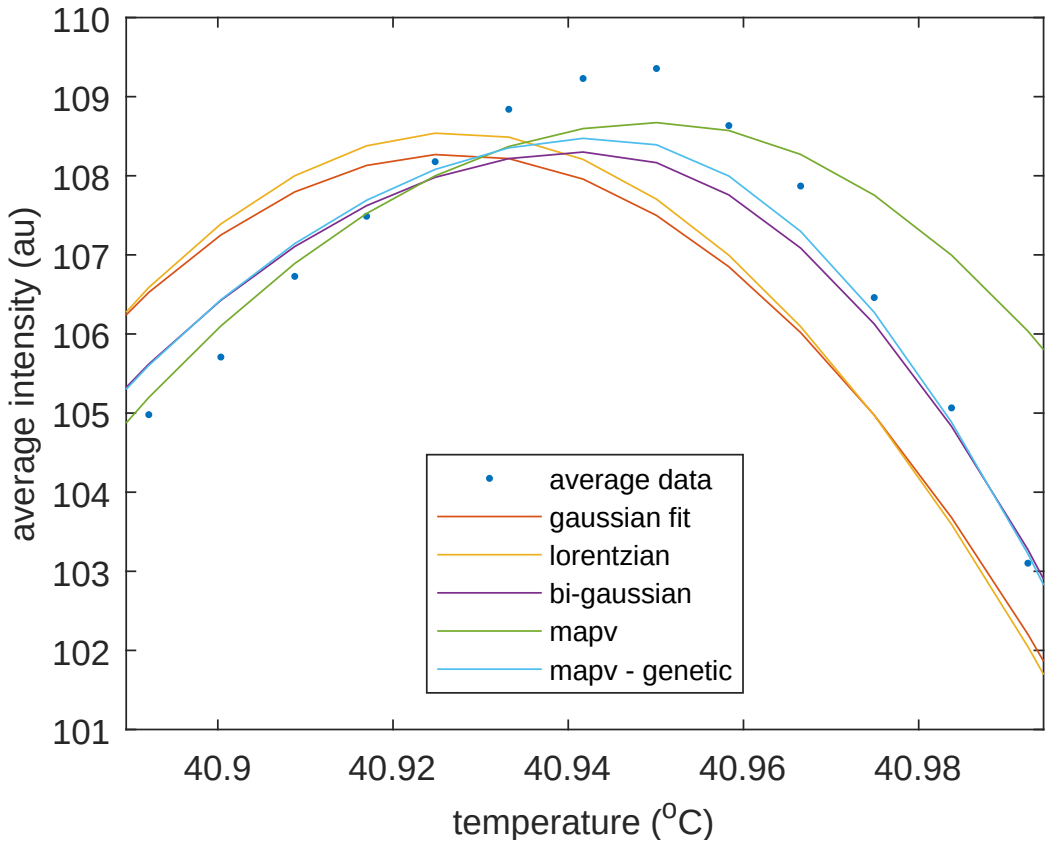

Figure 6. A comparison of the considered models, fitted to average intensity data.

Figure 6 displays some variation in the fitted summit location, T_{fit}, with the symmetric distribution summits located at lower temperatures compared to the average data. Because of the smoothness of the spatially averaged intensity data, a good integer (or time-step resolution) estimate of the true summit location is the maximum intensity value. A refinement of this is further reasonable, estimating the summit location to sub-integer resolution. Due to the low amplitude of noise within the spatially averaged data, a fully constrained fit of a second order polynomial was performed and used to interpolate the summit location. The integer estimate measures the summit location as $T_{int} = 40.9501 \pm 0.0087^oC$, whereas the sub-integer estimate measures the summit location as $T_{subint} = 40.9471^oC$, slightly to the left of the integer peak. This is confirmed as a reasonable estimate by inspection of the average data plotted in Figure 6. The error in the summit peak location fitted by the candidate models may then be estimated as $\varepsilon_T = |T_{subint} - T_{fit}|$. An appropriate model should find this peak location to better than integer resolution, or $\varepsilon_T < 0.0087^oC$. This condition may at first appear overly stringent, since temperature measurement uncertainties are estimated at $0.011\,^oC$. However, for the chosen model to fit the data adequately in the presence of noise, it must perform much better in the absence of it. Were an appropriate model fitted to the average data, the recovered regressed summit location would in reality be closer to the *true* summit

Table 1. A comparison of the appropriateness of the models investigated.

	Gaussian	Lorentzian	bi-Gaussian	mAPV	mAPV, genetic
$\varepsilon_T(^oC)$	0.020194	0.019939	0.005230	0.003061	0.003154
NRMSE (%)	4.400765	4.325366	2.429527	13.798281	1.902497
Time taken (s)	0.002769	0.001475	0.001711	0.008698	16.555759

location than that identified from the fully constrained polynomial fit performed, T_{subint}. Hence the lowest value of ε_T does not necessarily indicate the best possible model. For this reason, the range normalised root mean square error (NRMSE) of the fit is used as a benchmark to assess convergence. Finally, the time taken for the iterative solver to converge is used to assess the practical applicability of the models. This is because for this study the model will be used to find summit locations for many tens of thousands of peaks measured across the ROI. However, for application to complex geometries, millions of peak fitting processes will be required to be performed. The chosen model must therefore be capable of achieving this in timely fashion. These parameters are compared in Table 1.

Inspection of ε_T from Table 1 indicates that both the Gaussian and Lorentzian models fail to predict summit locations to better than integer (or time-step) precision. Both models result in errors of approximately 2.5 times integer resolution. This is additionally observed in Figure 6, where both the peaks of the Gaussian and Lorentzian curves lie to the left of the true summit location. This is believed to be an artefact of the inability of the models to parameterise the skewness of the underlying data. The NRMSE listed in Table 1 indicates significantly higher error from the resulting regression for the mAPV. This is again confirmed by Figure 6, which shows that data to the left hand side of the summit is reasonably well fitted, whereas data to the right hand side is poorly fitted. This suggests the low value of ε_T for this model is a coincidence. This form of fitting artefact is common for nonlinear least squares regression using gradient descent methods for cases where the model chosen contains more coefficients than are required to parameterise the underlying data. In this circumstance, a family of parameter combinations exist which locally minimise the error function, hence the optimised error surface contains multiple minima. Because of the notorious inability of the gradient descent optimiser to escape from local minima and find the optimal global minimum, invalid solutions to the regression are commonplace. This is likely the case for the mAPV and so is a poor candidate for application to large numbers of peak data, since many invalid regressions and so summit locations are to be expected. Replacing the gradient descent optimiser with a genetic algorithm search resolves this issue and so improves the performance of the fit, with the lowest values of ε_T and NRMSE measured. Unfortunately, due to the increased search intensity from this method, the time taken to fit a single peak is 3-4 orders of magnitude larger than for the gradient descent approach. For this reason, the bi-Gaussian model is identified as the most appropriate

of the models tested, providing better than time-step resolution of the summit location, low NRMSE and short regression times. It has therefore been used to fit the intensity summit location from the identified upper quartile of raw data.

4. Results

For each TLC tested, Figure 7 shows how the relationship between spatially averaged intensity and surface temperature varies with thermal cycling. This provides a statistically representative summary of the impact of ageing upon the returned light intensity across the ROI with temperature. As the number of cycles is increased, the average peak profile generally becomes both shallower and broader for all crystals, with summit locations shifting towards higher temperatures after large numbers of cycles. To investigate the mechanisms responsible for these results, the summit locations at each pixel location have been analysed as described in Sections 4.1 and 4.2. The trends observed are all outside of the bounds of experimental uncertainty, which is estimated at $0.014\,^oC$ based on the temperature measurement uncertainty of $0.011\,^oC$ and peak fitting uncertainty of $< 0.0087\,^oC$.

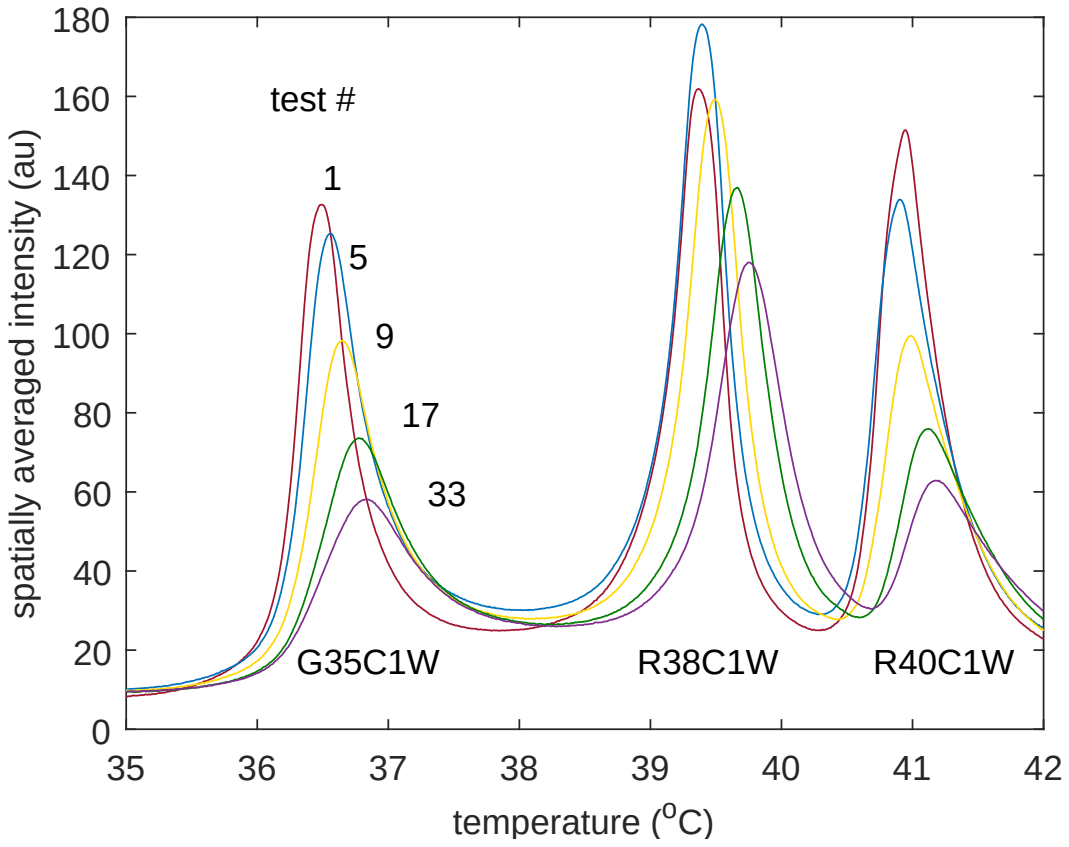

Figure 7. Spatially averaged profiles showing how TLC ageing impacts the relationship between measured intensity and temperature.

4.1. Summit location

The shift in summit location apparent from the spatially averaged data in Figure 7 corresponds to a change in the TLC response, with reflectance in the measured wavelength band moving to a different temperature. If a pre-determined calibration were used to relate the summit location to temperature, this would result in an error in the indicated surface temperature. The shift in summit location therefore represents a source of systematic temperature uncertainty that increases with the number of thermal cycles performed. Figure 8 shows this uncertainty, which has been calculated from the average of the summit locations measured at each of the 30000 pixels across the ROI. The same trend is evident for all three TLCs, with the summit location changing at an approximately linear rate across the first 20 cycles. Trend lines have been added to Figure 8 to illustrate the degree of linearity observed. At low numbers of cycles (≤ 5), the summit shifts to lower temperatures compared to the initial test, before moving to comparatively higher temperatures up to around cycle 20. Beyond cycle 20, more scatter is introduced to the data and no further increase in uncertainty is seen. Instead, the systematic uncertainties tend towards constant values of approximately $0.2 - 0.3\,^oC$. These values are slightly lower than those reported by Wiberg [13], who quoted ageing induced uncertainties of 0.5 and $2.2\,^oC$ for TLC film thickness of $38\,\mu m$ and $9\,\mu m$ respectively. However, these results apply to wide-band TLCs that were exposed to comparatively longer periods of heating (70-275 minutes) that are unlikely to occur in the context of transient heat transfer experiments, which are typically limited to 1-2 minutes. For narrow-band TLCs, Kakade [12] reported an ageing uncertainty of $0.3\,^oC$ for coatings of $30\,\mu m$ and $45\,\mu m$ thickness following similarly long periods of heating (150 minutes).

4.2. Peak profile

Based on the spatially averaged data plotted in Figure 7, a reduction in peak intensity of $\sim 56\%$ can be observed between the first and last thermal cycling tests. This closely matches the reduction of 60% reported by Kakade [12]. The reduction in peak height in Figure 7 is generally accompanied by an increase in peak width, which could have resulted from multiple artefacts in the individual time series recorded at any given pixel. Either the bandwidth of reflected wavelengths increases leading to greater peak widths with ageing, or individual crystals age at different rates resulting in a greater spread of summit locations. This can be evaluated directly by considering the variance of summit locations across the ROI, σ^2. Figure 9 shows the variance plotted in terms of random temperature uncertainty, which for the large sample represented by the ROI (30000 pixels) is defined as 2σ across a 95% confidence interval. Like the systematic uncertainty, the random uncertainty for all three crystals is seen to increase with the number of thermal cycles performed. This indicates that the increasing peak width observed in Figure 7 is caused by a greater spread of summit locations across the ROI with ageing. Examination of the PDFs of individual summit locations and peak widths across the

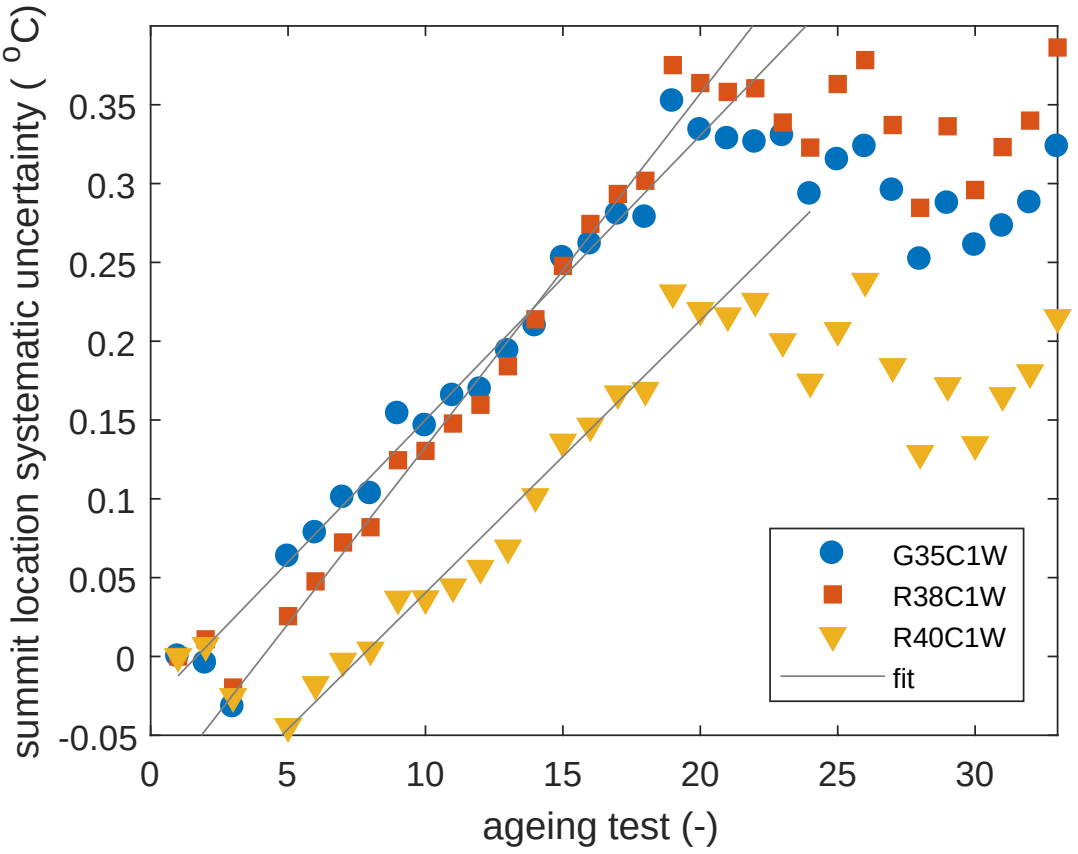

Figure 8. The impact of TLC ageing on systematic temperature uncertainty.

ROI confirms this result, with variations in summit location being the dominant effect. If a point calibration were applied globally across the measurement region, the random uncertainty in indicated surface temperature would therefore increase with ageing. The rate of increase is nominally linear and trend lines have again been fitted to the first 20 samples in Figure 9 to illustrate this. Some departure from the linear trend is observed from around test 14, with a greater level of scatter also becoming apparent in the data after test 20.

4.3. Crystal comparison

Based on the fits shown in Figures 8 and 9, Table 2 compares the rate of increase in random and systematic uncertainties over the first 20 thermal cycles for all three TLCs. The rate of change of systematic uncertainty is highest for R38C1W and lowest for R40C1W, while the rate of change of random uncertainty is highest for G35C1W and lowest for R38C1W. When random and systematic uncertainty contributions are combined using a root-sum-square method, the lowest expanded uncertainty of $0.26\,^oC$ is found for crystal R40C1W, compared to $0.37\,^oC$ and $0.38\,^oC$ for crystals G35C1W and R38C1W respectively. These results reveal no correlation between cycling temperatures

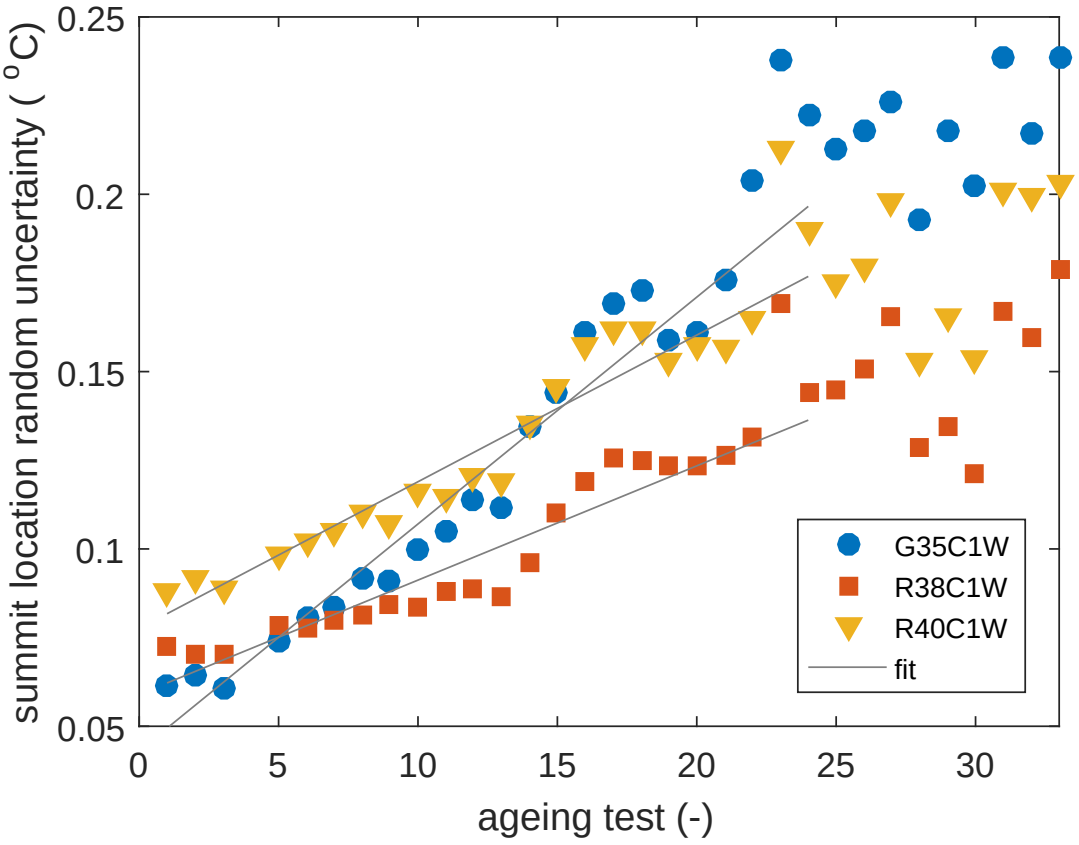

Figure 9. The impact of TLC ageing on random temperature uncertainty.

and the temperature range over which the TLC is active. Furthermore, none of the crystals exceeded their upper clearing temperatures of $> 65\,^oC$ during the thermal cycles. This suggests that ageing effects are determined by other factors.

Table 2. The rate of change of uncertainty with ageing.

	G35C1W	R38C1W	R40C1W
Systematic uncertainty (^oC)	0.018043	0.022430	0.014849
Random uncertainty (^oC)	0.006396	0.003222	0.004135

4.4. Uncertainty propagation

In transient heat transfer experiments, the ageing induced uncertainties plotted in Figures 8 and 9 would act to progressively increase the uncertainty in surface temperature indicated by the TLC colour-play. The impact of this increased uncertainty on calculated HTCs can be determined using the Taylor series method of uncertainty propagation [27]. For the problem of a one-dimensional semi-infinite plate subject to a

step temperature change in fluid temperature [8]:

$$\left(\frac{P_h}{h}\right)^2 = \left(\frac{P_\alpha}{\alpha}\right)^2 + \left(\frac{1}{2}\frac{P_t}{t}\right)^2 + \left(\frac{1}{2}\frac{P_\kappa}{\kappa}\right)^2 \tag{4}$$

where

$$\left(\frac{P_\alpha}{\alpha}\right)^2 = \left(\frac{1}{\alpha f'(\alpha)}\right)^2 \left[\left(\frac{P_{T_w}}{T_\infty - T_i}\right)^2 + (1-f(\alpha))^2 \left(\frac{P_{T_i}}{T_\infty - T_i}\right)^2 + f^2(\alpha)\left(\frac{P_{T_\infty}}{T_\infty - T_i}\right)^2\right] \tag{5}$$

$$f(\alpha) = 1 - e^{\alpha^2} erfc(\alpha) \tag{6}$$

$$f'(\alpha) = 2\left[\alpha(f(\alpha)-1) + \pi^{-1/2}\right] \tag{7}$$

Eq. 4 is written in terms of random uncertainties, but may also be applied for systematic uncertainties assuming there are no correlated uncertainty sources. This assumption is valid if only the ageing induced uncertainty in surface temperature is considered and all other experimental uncertainty sources (e.g. t, κ) are neglected. This approach is selected to give the clearest indication of the impact of ageing induced uncertainties on calculated HTCs, since other sources of uncertainty will vary between different experimental arrangements.

With random and systematic uncertainties calculated from Eq. 4, the expanded uncertainty in HTC due to ageing effects can finally be determined from Eq. 8. This is the 95% confidence large sample uncertainty estimate [27]:

$$\left(\frac{U_h}{h}\right)^2 = \left(\frac{P_h}{h}\right)^2 + \left(\frac{B_h}{h}\right)^2 \tag{8}$$

Figure 10 shows the expanded uncertainty in HTC that can be attributed to TLC ageing after 20 cyclic tests. Data is presented for a range of normalised temperature ratios (Eq. 9), using a fixed free-stream temperature and ambient initial conditions. The different temperature ratios therefore represent the different surface temperatures and corresponding rates of heat transfer that may be encountered in an experiment. For complex cooling geometries, these ratios are expected to cover a wide range of values due to the large spatial variations in HTC. The normalised temperature ratio is defined by:

$$\Phi = \frac{T_w(t) - T_i}{T_\infty - T_i} \tag{9}$$

For crystals G35C1W and R38C1W, the uncertainty in HTC due to TLC ageing varies from 3.4% to 5.6% between $\Phi = 0.2$ and $\Phi = 0.8$. For R40C1W, this ageing induced uncertainty drops by $1-2\%$. The sensitivity to normalised temperature ratio arises from the leading term in Eq. 5, which is an amplification factor that depends on α

and has a minimum value at $\Phi \approx 0.5$. According to Yan and Owen [8], an overall HTC uncertainty of 2.5% would be regarded as acceptable by most experimenters. Given that all other sources of experimental uncertainty are excluded in the current analysis, the situation shown in Figure 10 is clearly unsatisfactory. For experiments involving a large number of thermal cycles, means of mitigating TLC ageing effects must therefore be considered if accurate HTC distributions are to be determined.

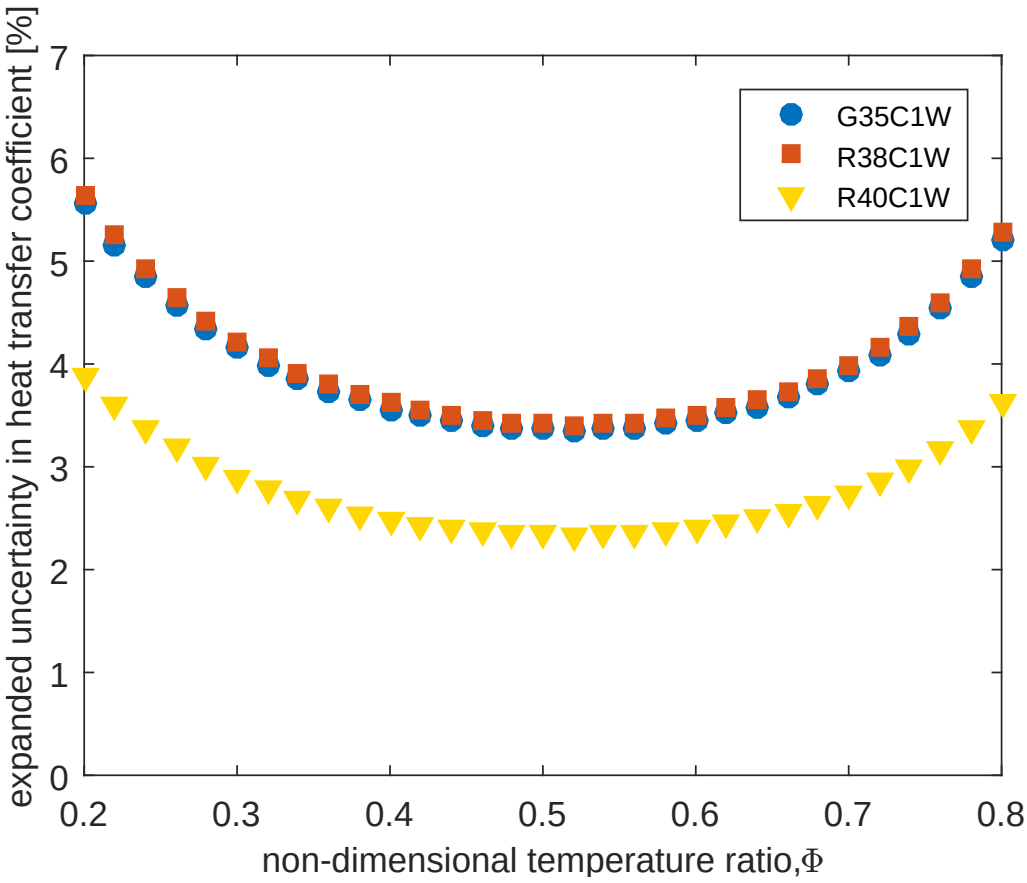

Figure 10. Expanded uncertainty in heat transfer coefficient due to random and systematic ageing effects

4.5. Ageing mitigation strategies

One approach to reducing uncertainties introduced by TLC ageing is to correct for the systematic uncertainty in surface temperature that is introduced by the shifting summit location in TLC reflected intensity. This is easily achieved if a thermocouple is attached to the measurement surface and its output used to adjust the colour-temperature calibration for each cyclic test. Since the colour-temperature calibration is applied globally across the measurement surface, this correction would only be valid if all regions of the TLC aged identically, which may not be the case in complex cooling geometries where large spatial temperature variations are present. In this circumstance,

it may be more logical to artificially age the TLC prior to the experimental campaign by exposing it to a sufficient number of thermal cycles (> 20) such that no further shift in summit location is observed. The successful application of either of these techniques would limit the uncertainty introduced by ageing to the random temperature uncertainty reported in Section 4.2. Figure 11 shows the subsequent reduction in HTC uncertainty that would be achieved in this scenario, which is approximately one half of the value attained without correction. Beyond this reduction, no further improvement in HTC uncertainty is achievable without removing and reapplying the TLC coating in order to decrease the contribution of the random temperature uncertainty.

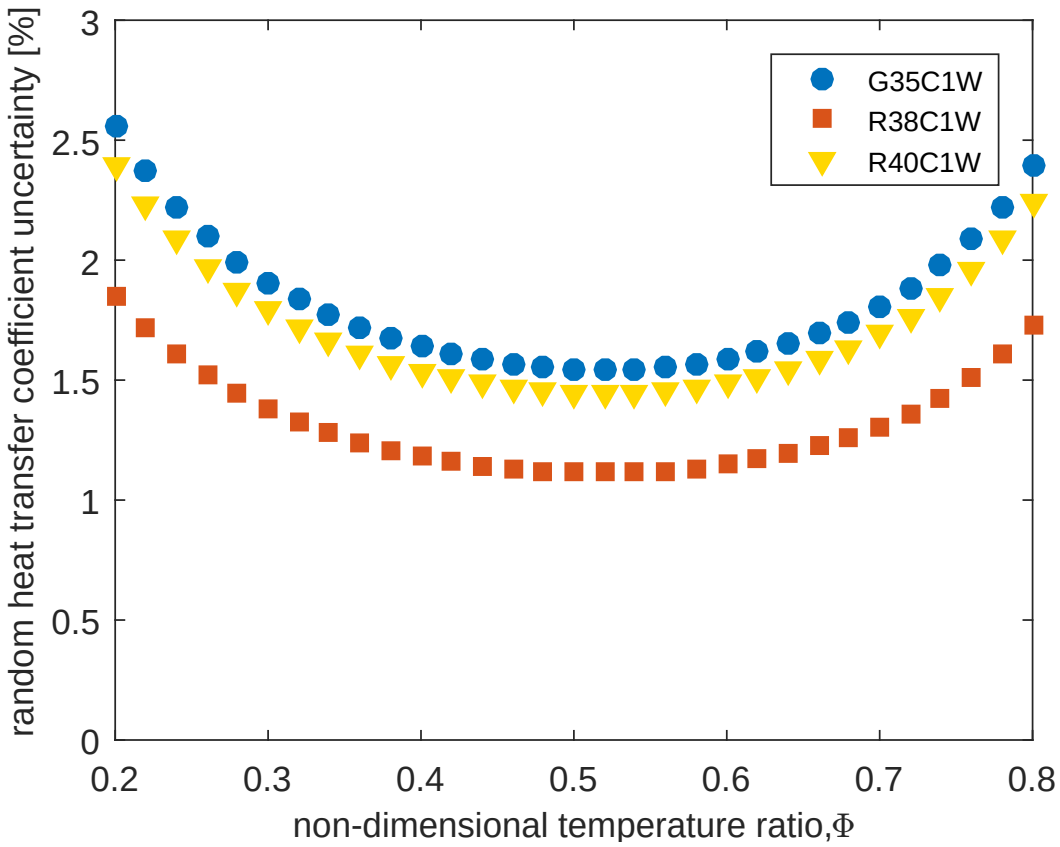

Figure 11. Uncertainty in heat transfer coefficient due to random ageing effects only

4.6. Spatial variations

Since random uncertainties introduced by TLC ageing still have a significant impact on HTC accuracy, the spatial variations in TLC colour-play that give rise to these uncertainties have been analysed in further detail. Figure 12 illustrates the evolution of indicated surface temperature fields, extracted from the ROI. Each column of Figure 12 corresponds to a different TLC and each row to different thermal cycling test. The previously described increase in systematic uncertainty is apparent, with a

shift towards higher temperatures as the test number increases. Further to this, the indicated temperature fields additionally exhibit some high-frequency noise and also some underlying structure, dependant upon the number of ageing tests performed.

4.6.1. Structured patterns The structures observed in Figure 12 become prominent around test 14, with the appearance of a pattern of lines in the temperature field. The lines are consistently observed for all three crystals and are much larger than the measurement resolution, at $\sim 0.5mm$ across and $\sim 5mm$ long. The measured patterns evolve over time, increasing in length, width, frequency and maximum temperature. After a few thermal cycles, some of the observed lines merge, becoming almost arterial in appearance. Because of the higher temperatures (by $0.25 - 0.3^oC$) measured local to these patterns, there will be a consequent increase in the spatial standard deviation and hence random temperature uncertainty. This is apparent in Figure 9, where an increase in uncertainty and consequent departure from the linear trend can be observed at around test 14.

Investigations into the origins of the linear patterns in the temperature fields have been performed. By quantifying the peak height for the affected tests, an assessment can be made of whether the structure observed is an ageing phenomenon or related to some form of experimental error. Since the peak height is well known to decrease with ageing, any variation of ageing effects within the field must similarly result in variations in peak height. Upon inspection of Figure 13, no such peak height variations are apparent and hence the linear patterns observed in Figure 12 cannot be attributed to ageing. Alternatively, the patterns could be related to delamination of the TLC coating due to the effects of thermal expansion. However, this is characterised by a flaky appearance to the coating and no evidence of this was visible on the sample surface. Instead, the most likely cause of the patterns is considered to be discontinuities in the layer of thermal grease between the copper block and acrylic disc. It is believed that small movements resulting from thermal expansion/contraction led to localised pockets where good thermal contact with the copper block was lost. These regions spread with repeated cycling, resulting in the observed patterns. This effect, whilst appearing prominent in the field plots shown in Figure 12, actually makes relatively little contribution to the overall random temperature uncertainty. The trend of increasing random uncertainty with TLC ageing is therefore unchanged.

4.6.2. High-frequency noise The high-frequency noise observed in Figure 12 occurs nominally at the pixel scale. Occurrences of this manifest before test 6, appearing as a granular structure, with intermittent saturation. The structure observed is inconsistent between the three TLCs, with this being particularly clear in cases where the colour scale results in saturation of the indicated temperature. The observed spatial frequency increases with the number of thermal cycles performed, with the effect being most pronounced for G35C1W and least significant for R38C1W. This is consistent with the observed trends in random uncertainty in Figure 9. As has been extensively discussed,

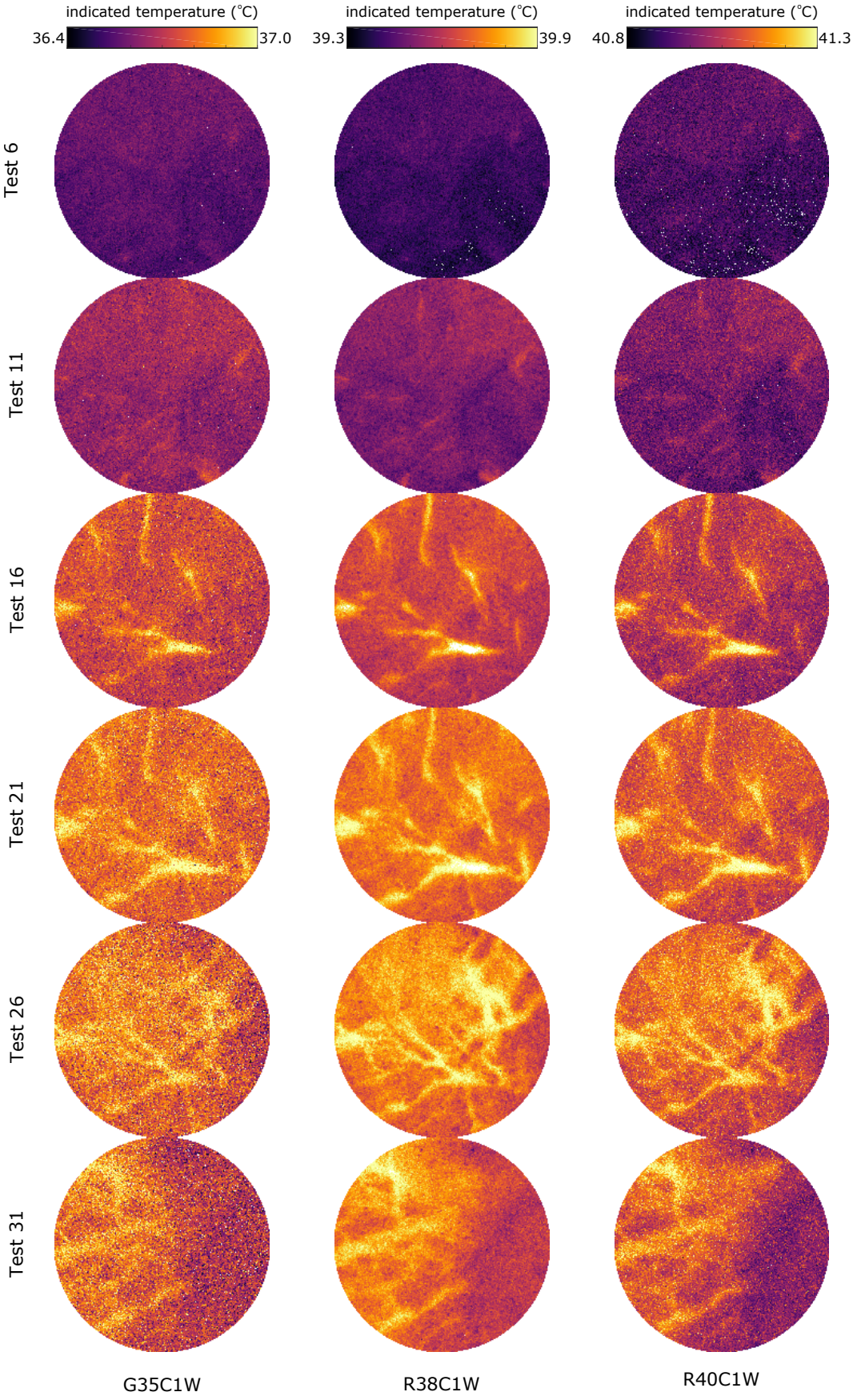

Figure 12. Spatial variation of TLC ageing.

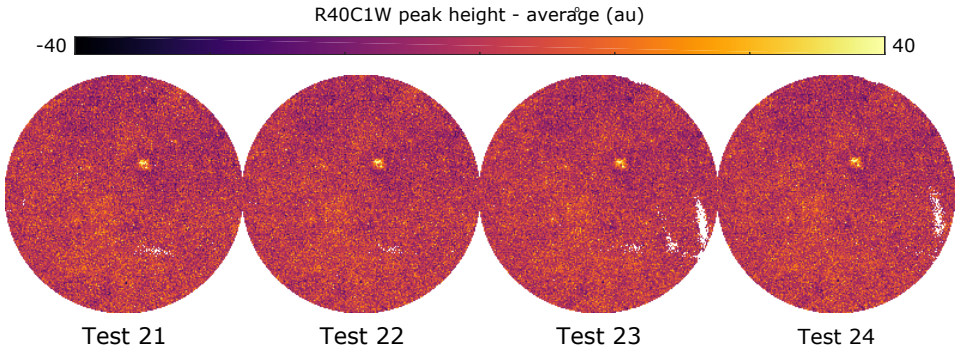

Figure 13. Spatial variation of measured peak height, mean subtracted.

the intensity signal decreases with ageing, resulting in a decrease in the imaged peak height and so the signal to noise ratio of the corresponding bi-Gaussian fit used to extract summit location data. It is therefore possible that the occurrence of this high frequency noise, and so a portion of the increase in random uncertainty identified in Figure 9, results simply from an increase in the measurement error associated with peak fitting. Some noise is expected in any camera application, typically a combination of dark and read noises. As the measured signal decreases so too does the measurement noise, but this is rarely proportional, hence at low intensities a higher percentage of noise in the image is expected.

Figures 14 and 15 show the mean and standard deviation of the NRMSE of the fits performed with evolving ageing. This shows the expected trend of increased fitting error with ageing, corresponding to a reduction in SNR due to reduced peak height. Comparisons between the different TLCs indicate that there is no correlation between high NRMSE and either random or systematic temperature uncertainties. For example, R40C1W exhibits the highest mean and standard deviation NRMSEs, yet is associated with the lowest systematic uncertainty in Figure 8. Similarly, the increase in scatter observed in Figures 8 and 9 for > 20 cyclic tests is not reflected in the NRMSE data, which would otherwise have suggested decreased fitting performance and failure of the data processing techniques to accurately identify peak locations. A small increase in the mean and standard deviation NRMSE occurs around test 21, but within 3-4 tests the values have returned to trend. Were there to have been sufficient deterioration of the peak SNR for peak fitting to generally fail, it would be expected that both the mean and standard deviation NRMSE would rapidly increase and show some significant scatter. This does not occur, confirming that the trends observed in random and systematic temperature uncertainty originate from actual variations in the TLC due to ageing, rather than measurement errors due to peak fitting.

To further investigate the origins of the high frequency noise apparent in Figure 12, analyses were made of the time evolution of the raw image data by manually inspecting the mean subtracted intensity fields at fixed dynamic. This demonstrated that for later aged samples, especially for G35C1W, small groups of pixels indicated significantly later (and so at higher temperatures) than in tests where less ageing had occurred.

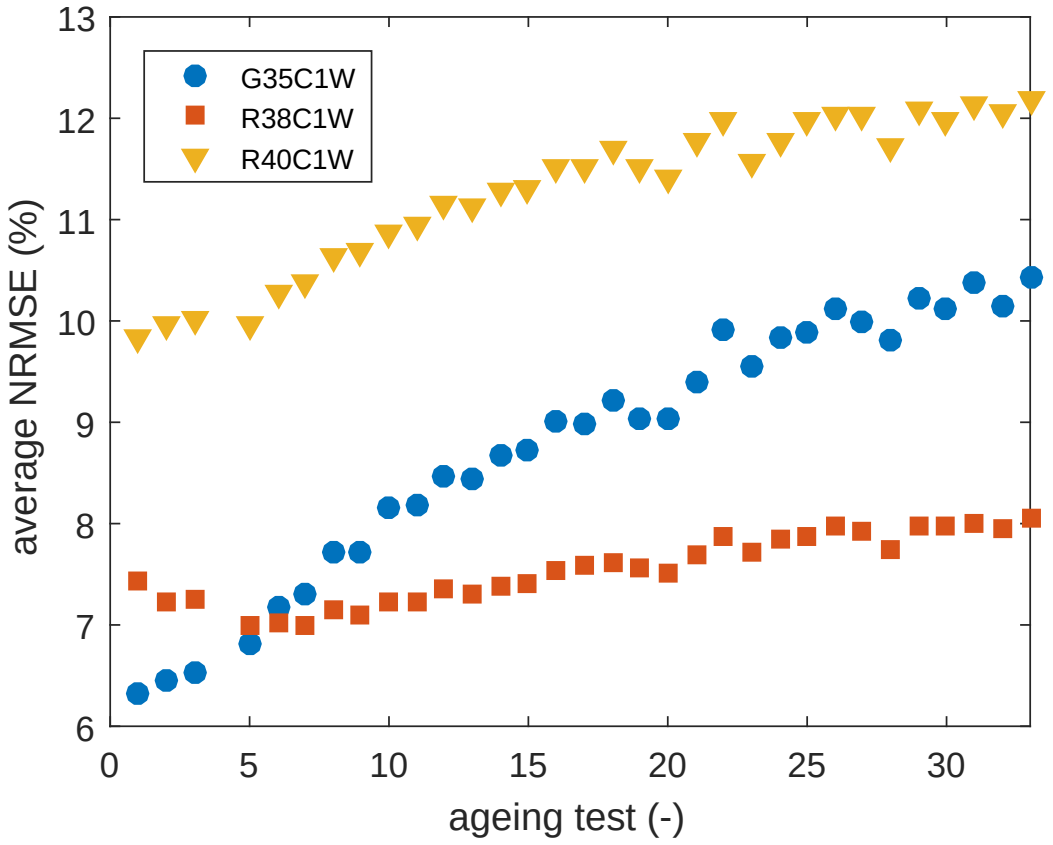

Figure 14. The impact of ageing on sub-integer peak detection performance, mean NRMSE.

Particularly prominent cases were especially identifiable, because they would indicate outside of the main intensity peaks, in the trough region between TLCs. By viewing image data in this way, the CCD noise was also discernible. This was because the high spatial frequency pattern remained fixed in time, apparently related to a small scale imaged phenomena, such as the deposited crystal structure. The sensor noise was manifested, superimposed onto this pattern as a low amplitude intensity fluctuation in time.

For the imaging configuration used, the object plane resolution was $\mathcal{O}100\mu m$, whereas TLC microcapsule sizes were in the range $10 - 30\mu m$. Because of the relative size of the microcapsules compared to the imaging resolution, relatively small numbers of microcapsules are expected to be imaged by any given pixel. It is reasonable to assume therefore that the high resolution of the imaging system results in insufficiently large numbers of microcapsules being imaged to render a homogeneous field. This implies that the high frequency artefacts observed in the recorded images result from changes to the individual TLCs. The 10 count rejection threshold discussed in Section 3 effectively eliminates low level reflections from the non-temperature dependant elements of the test sample, supporting this hypothesis. Furthermore, inspection of the raw data fields

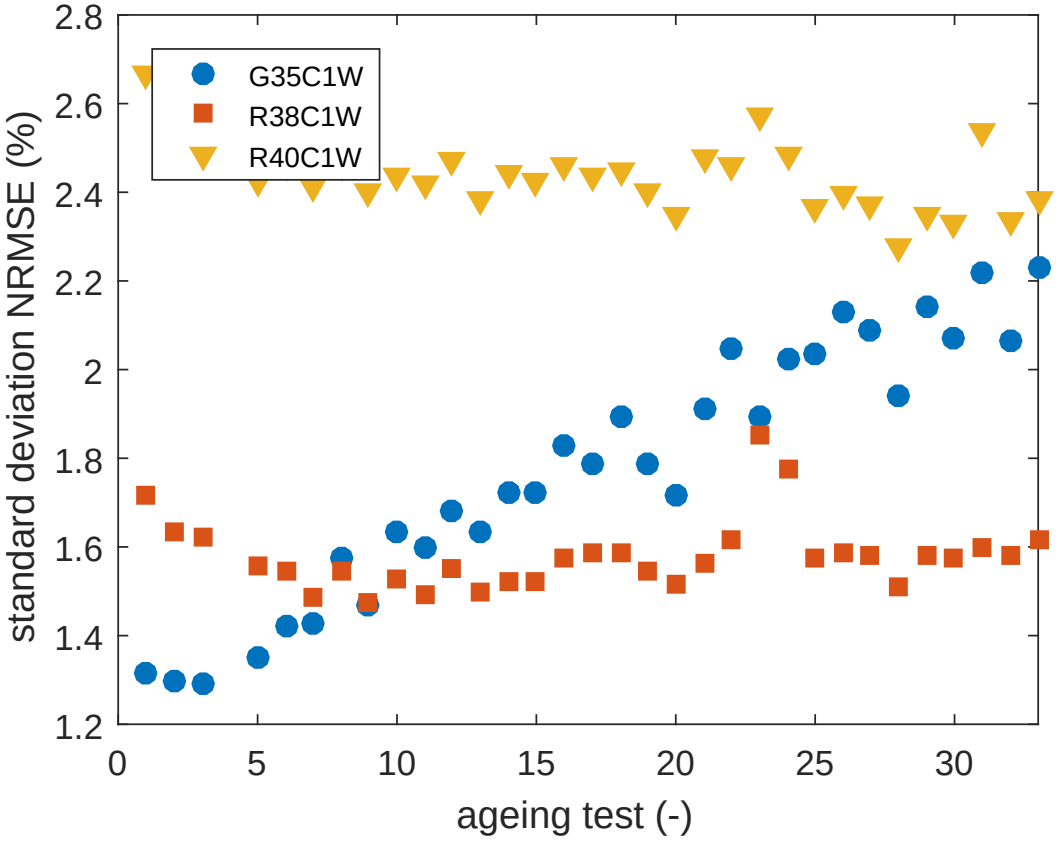

Figure 15. The impact of ageing on sub-integer peak detection performance, standard deviation of NRMSE.

indicates that there is no significant change to the frequency of the underlying granular structure observed in the images. This in turn suggests that ageing has not caused the refractive index or scattering properties of the microcapsules/binder to change significantly, altering the light path reflected by the TLCs. It seems logical therefore to conclude that the high frequency variations in the temperature field result from changes to individual crystals or crystal clusters. The fact that the average temperature change is gradual, but simultaneously some sporadic, sudden ageing is apparent, suggests some probability of any given crystal or crystal cluster ageing.

5. Conclusion

In this work, TLC ageing effects have been quantified using a new monochrome imaging system and peak detection methodology that are optimised for the intensity-based method of analysing TLC thermography data. Repeated thermal cycling between $30\,^oC$ and $45\,^oC$ has been shown to cause the average peak summit location to shift, with reflectance in the measured wavelength band moving to temperatures $0.2-0.3\,^oC$ higher after ~ 20 tests. This summit shift is accompanied by a flattening and broadening of

the average peak profile, which corresponds to a $\sim 60\%$ reduction in reflected intensity and an increased variance in summit locations among individual crystals. These trends result in increased random and systematic uncertainties in the surface temperatures derived from summit location measurements. When these sources of uncertainty are combined after $\sim$ 20 thermal cycles, the lowest expanded uncertainty of $0.26\,^oC$ is found for crystal R40C1W, compared to $0.37\,^oC$ and $0.38\,^oC$ for crystals G35C1W and R38C1W respectively. This result reveals no correlation between ageing and either the TLC active temperature range or upper clearing temperature, which might otherwise have been expected from literature. In a transient heat transfer experiment, the ageing induced uncertainties measured here would give rise to calculated HTC uncertainties of up to 5.6% after $\sim$ 20 cyclic tests. This outcome is of particular concern for experiments involving complex gas turbine cooling geometries, where many repeated tests are required to capture the multiple images needed to establish complete surface HTC distributions. To mitigate ageing effects, it is recommended that either global colour-temperature calibrations be continuously updated to account for the shifting summit location or the crystal be artificially aged such that no further summit shift is observed. Both of these approaches would see ageing induced uncertainties in HTC halved to values of up to 2.6%. This residual uncertainty originates from random uncertainty contributions, which cannot be eliminated since they are attributed to changes in individual crystals or crystal clusters with ageing. It should be remembered that the present study has only addressed the impact of repeated thermal cycling on TLC ageing, and sensitivity to other cycle parameters such as the temperature, duration and rate of heating has not be quantified. These parameters require further investigation as they could lead to variations in ageing induced uncertainties for different experimental arrangements. The repeatability of the measured ageing effects should also be examined, preferably with some improved means of maintaining thermal contact between the TLC sample and the copper block.

Acknowledgements

This work was jointly funded by the EPSRC and Rolls-Royce plc. as part of the Centre for Doctoral Training in Gas Turbine Aerodynamics. The authors would like to thank Stephen Harding from Rolls-Royce plc. for supporting this work.

Nomenclature

B	systematic uncertainty
C	solid specific heat capacity
$erfc$	complementary error function
h	heat transfer coefficient
k	solid thermal conductivity
t	time

P random uncertainty
T temperature
U expanded uncertainty
z peak width at half-height

Subscripts

fit fitted value
i initial (t=0)
int estimated to integer resolution
$subint$ estimated to sub-integer resolution
w evaluated at the surface
∞ evaluated in the free-stream

Greek letters

α non-dimensional heat transfer coefficient ($h\sqrt{(t/\kappa)}$)
ϵ peak fitting error
κ solid thermal properties (ρCk)
ρ solid density
ϕ normalised temperature ratio
σ standard deviation

References

[1] Savarianandam V, Thorpe S J, Carrotte J F and Zedda M 2012 An investigation of an impingement/pin-fin cooling system for gas turbine combustor applications *ASME Turbo Expo 2012: Turbine Technical Conference and Exposition* (American Society of Mechanical Engineers) pp 871–880
[2] Batstone J, Gillespie D and Romero E 2011 Detailed local heat transfer measurements in a model of a dendritic gas turbine blade cooling design *ASME 2011 Turbo Expo: Turbine Technical Conference and Exposition* (American Society of Mechanical Engineers) pp 389–398
[3] Bunker R S 2013 Gas turbine cooling: Moving from macro to micro cooling *Volume 3C: Heat Transfer* (ASME) p V03CT14A002
[4] Ireland P T, Neely A J, Gillespie D R and Robertson A J 1999 *Int. J. Heat Fluid Flow* **20** 355–367
[5] Gillespie D R H, Wang Z, Ireland P T and Kohler S T 1998 *J. Turbomach.* **120** 92–99
[6] Neely A J, Ireland P T and Harper L R 1997 *Proceedings of the Institution of Mechanical Engineers, Part A: Journal of Power and Energy* **211** 273–287
[7] Wang Z, Ireland P T, Kohler S T and Chew J W 1998 *J. Turbomach.* **120** 63–69
[8] Yan Y and Owen J M 2002 *International Journal of Heat and Fluid Flow* **23** 29–35
[9] Terzis A, Bontitsopoulos S, Ott P, von Wolfersdorf J and Kalfas A I 2016 *J. Turbomach.* **138** 021003
[10] Sabatino D R, Praisner T J and Smith C R 2000 *Exp. Fluids* **28** 497–505
[11] Poser R, von Wolfersdorf J and Lutum E 2007 *Proceedings of the Institution of Mechanical Engineers, Part A: Journal of Power and Energy* **221** 793–801
[12] Kakade V, Lock G, Wilson M, Owen J and Mayhew J 2009 *Int. J. Heat Fluid Flow* **30** 939–949
[13] Wiberg R and Lior N 2004 *Rev. Sci. Instrum.* **75** 2985–2994
[14] Anderson M R and Baughn J W 2004 *J. Heat Transfer* **126** 339–346
[15] Stasiek J, Stasiek A, Jewartowski M and Collins M 2006 *Optics & Laser Technology* **38** 243–256
[16] Baughn J W, Anderson M R, Mayhew J E and Wolf J D 1999 *J. Heat Transfer* **121** 1067–1072

[17] Kodzwa P M, Elkins C J, Mukerji D and Eaton J K 2007 *Exp. Fluids* **43** 475–486
[18] Rao Y and Zang S 2010 *Meas. Sci. Technol.* **21** 015105
[19] Waidmann C, Poser R and von Wolfersdorf J 2013 Application of thermochromic liquid crystal mixtures for transient heat transfer measurements *10th European Conference on Turbomachinery Fluid Dynamics and Thermodynamics, ETC 2013* ETC2013-017 pp 685–696
[20] Schulz S, Brack S, Terzis A, von Wolfersdorf J and Ott P 2016 *Exp. Therm Fluid Sci.* **70** 196–207
[21] Babinsky H and Edwards J A 1996 *Exp. Fluids* **21** 227–236
[22] Chan T, Ashforth-Frost S and Jambunathan K 2001 *Int. J. Heat Mass Transfer* **44** 2209–2223
[23] Poole C F 2003 *The essence of chromatography* (Elsevier)
[24] Di Marco V B and Bombi G G 2001 *Journal of Chromatography A* **931** 1–30
[25] Buys T and De Clerk K 1972 *Analytical Chemistry* **44** 1273–1275
[26] Wijetunge C D, Saeed I, Boughton B A, Roessner U and Halgamuge S K 2015 *BMC Genomics* **16** S12
[27] Coleman H W and Steele W G 1995 *The American Institute of Aeronautics and Astronautics Journal* **33** 1888–1896